Comparison of CFD Analysis to Empirical Data in a Commercial Vortex Tube

H. M. Skye, G. F. Nellis[+], S.A. Klein

Department of Mechanical Engineering, University of Wisconsin, Madison
1339 Engineering Research Building, 1500 Engineering Dr.
Madison, WI 53706
[+]corresponding author

gfnellis@engr.wisc.edu
Phone: (608) 265-6626
Fax: (608) 262-8464

Abstract

This paper presents a comparison between the performance predicted by a computational fluid dynamic (CFD) model and experimental measurements taken using a commercially available vortex tube. Specifically, the measured exit temperatures into and out of the vortex tube are compared with the CFD model. The data and the model are both verified using global mass and energy balances. The CFD model is a two-dimensional (2-D) steady axisymmetric model (with swirl) that utilizes both the standard and renormalization group (RNG) k-epsilon turbulence models. While CFD has been used previously to understand the fluid behavior internal to the vortex tube, it has not been applied as a predictive model of the vortex tube in order to develop a design tool that can be used with confidence over a range of operating conditions and geometries. The objective of this paper is the demonstration of the successful use of CFD in this regard, thereby providing a powerful tool that can be used to optimize vortex tube design as well as assess its utility in the context of new applications.

Nomenclature

A	Area (mm^2)
c_p	Constant pressure specific heat capacity of air at room temperature ($kJ\,kg^{-1}\,K^{-1}$)
E_{error}	Non-dimensional experimental energy balance error
L1, L2	Nozzle photograph measurements for determining inlet location
$\dot{m}$	Mass flow rate ($kg\,s^{-1}$)
$\dot{Q}$	Power separation (kW)
T	Temperature (K)
V	Velocity ($m\,s^{-1}$)

Greek Symbols

$\delta\dot{Q}$	Uncertainty in power separation (kW)
θ	Nozzle angle defining velocity vectors (degree)

Subscripts

c	Cold stream
h	Hot stream
in	Inlet
m	Model
n	Normal
r	Radial
tot	Total
θ	Tangential

Keywords

vortex tube, experimental verification, computational fluid dynamic, design

1. Introduction

Since their accidental discovery early in the 20th century, vortex tubes have fascinated researchers who have debated over the exact mechanism that drives the observed power separation (also called energy separation) phenomena. Despite an incomplete understanding of vortex tube physics, these devices are currently in production for a variety of commercial applications. Vortex tubes are typically used for their cooling capability in processes such as welding, brazing, solidifying polymers, and controlling air climate. While somewhat inefficient as a cooling device, vortex tubes can be useful in certain situations as they are small, simple to make and repair, and require no electrical or chemical power input.

Recent efforts have successfully utilized computational fluid dynamics (CFD) modeling to explain the fundamental principles behind the energy separation produced by the vortex tube. Frohlingsdorf et al. [1] modeled the flow within a vortex tube using a CFD solver that included compressible and turbulent effects. The numerical predictions qualitatively predicted the experimental results presented by Bruun [2]. Ahlborn et al. [3] [4] show the dependence of vortex tube performance on normalized pressure drop with a numerical model. Aljuwayhel et al. [5] successfully utilized a CFD model of the vortex tube to understand the fundamental processes that drive the power separation phenomena. This paper presents a comparison of the power separation effect in a commercial vortex tube with a CFD model similar to that in [5].

CFD models have not been utilized as design tools for vortex tubes, in part because their predictive ability in this regard has not previously been demonstrated. The objective of this paper is to demonstrate the ability of a carefully implemented CFD model to predict the measured performance of a commercial vortex tube over a range of parameters. The motivation for this work is the development of a tool that will allow researchers to use CFD to understand effects of modifying the geometry of a vortex tube without resorting to the manufacture and test of numerous design permutations. Also, the performance of vortex tubes under operating conditions other than with the typical, room temperature compressed air can be evaluated and assessed relatively easily with a CFD model, allowing the investigation of the utility of the vortex tube in the context of new applications.

The experimental verification of the model focuses on comparisons between the temperature and power separation that is predicted by the CFD model and measured experimentally as the cold fraction is varied. The cold fraction is defined as the fraction of the inlet mass flow that exits the cold end of the tube. The validity of the experimental measurements is evaluated through an overall energy balance that is enabled by the simultaneous measurement of all of the inlet and exit mass flow rates and temperatures; the data set that is selected for comparison is confined to those points where the experimental energy balances close to within 10% Values falling outside this range are found at the extremes of high and low cold fractions where the total measurable temperature separation and exiting volume flows are low, resulting in a large uncertainty in the measured power separation.

2. Experimental Data

An Exair® 708 slpm (25 scfm) vortex tube was used to collect all of the experimental data reported here; the raw data can be found in Appendix 1. The vortex tube was energized with compressed air at a nominal inlet gauge pressure of 483 kPa (70 psig). The valve that typically controls the hot exit pressure of the vortex tube was removed; instead, a valve on the rotameter located downstream of the hot exit was used to control the hot exit pressure in this experiment in order to facilitate the measurement of this pressure. A schematic of the setup and list of equipment is shown in Fig. 1, and the range and accuracy of the equipment is listed in Table 1.

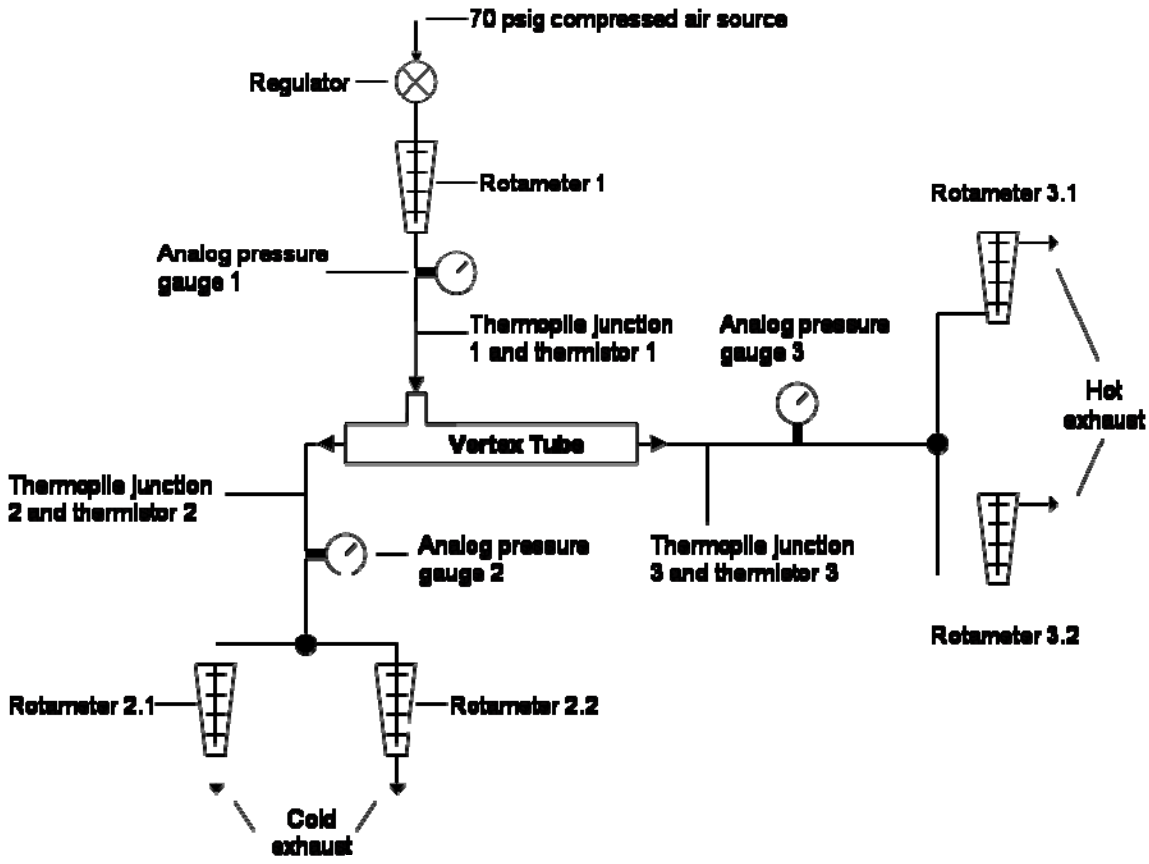

Figure 1: Schematic of the experimental test setup showing the location of key instrumentation.

Measurements of the volume flow rate were taken immediately before the inlet and at both exits of the vortex tube using variable area rotameters. A heat exchanger was used to cool the air exiting the hot side of the vortex tube in order to protect the rotameter. The rotameters that measured the flow leaving the vortex tube were vented to atmosphere and therefore atmospheric pressure (measured using a barometer) was used to determine the actual density at these locations. The density and volumetric flow rate together were used to obtain the mass flow rate ($\dot{m}$) associated with each of the respective streams.

Pressure measurements were taken using analog pressure gauges. The absolute values of the inlet and exit temperatures were measured with thermistors that were inserted into the fluid stream. The inlet-to-hot exit and inlet-to-cold exit temperature differences were also measured directly using two, 5-junction thermopiles composed of types T and E thermocouple wire, respectively. The thermopile junctions were also inserted into the fluid stream and were calibrated in situ prior to running the experiment. Evaluation of

the uncertainties of these temperature measurements indicated that the thermistors were more accurate for measuring the temperature differences than the thermopiles, although the results measured using each technique agreed to within the experimental error. All temperature values are assumed to be total temperatures as the thermopiles and thermistors create a stagnation point in the flow.

The power separation that is induced in the hot and cold streams that exit the vortex tube ($\dot{Q}_h$ and $\dot{Q}_c$, respectively) are calculated according to:

$$\dot{Q}_h = \dot{m}_h \, c_p (T_h - T_{in}) \tag{1}$$

$$\dot{Q}_c = \dot{m}_c \, c_p (T_{in} - T_c) \tag{2}$$

where $\dot{m}_h$ and $\dot{m}_c$ are the hot and cold mass flow rates, respectively, T_h, T_c, and T_{in} are the hot exit, cold exit, and inlet temperatures, respectively, and c_P is the specific heat capacity of air which is assumed to be constant and evaluated at room temperature.

In the absence of any parasitic heat gain or loss, the power separation calculated according to Eqs. (1) and (2) should be equal; therefore, the total power separation ($\dot{Q}_{tot}$) determined experimentally is taken to be the average of $\dot{Q}_h$ and $\dot{Q}_c$.

$$\dot{Q}_{tot} = \frac{\dot{Q}_c + \dot{Q}_h}{2} \tag{3}$$

The theoretical relative uncertainty of the total power separation ($\delta\dot{Q}_{tot}$) measured in the experiment is calculated based on the equipment accuracy listed in Table 1.

$$\frac{\delta\dot{Q}_{tot}}{\dot{Q}_{tot}} = \sqrt{\frac{\delta\dot{Q}_c^{\,2} + \delta\dot{Q}_h^{\,2}}{\left(\dot{Q}_h + \dot{Q}_c\right)^2}} \tag{4}$$

where $\delta\dot{Q}_h$ and $\delta\dot{Q}_c$ are the theoretical errors in the power separations calculated using Eqs. (1) and (2). The error in the experiment is calculated based on the deviation of the separately measured power flows from an overall energy balance. Since there are no heat or work inputs to the device, the difference in the

energy separation terms represents the energy balance error in the experiment. The non-dimensional energy balance error (E_{error}) is thus defined as:

$$E_{error} = \frac{1}{2}\left|\frac{\dot{Q}_h - \dot{Q}_c}{\dot{Q}_h + \dot{Q}_c}\right| \tag{5}$$

At the upper and lower limits of the cold fraction, the energy transfer rate ($\dot{Q}_h$ or $\dot{Q}_c$), approaches zero. As a result, both the theoretical uncertainty in the measurements as well as the experimentally determined energy balance error, defined by Eq. (5), increase sharply. Fig. 2 illustrates the theoretical relative uncertainty in the measurement as well as the measured energy balance error (i.e., the results of Eqs. (4) and (5)) as a function of the cold fraction.

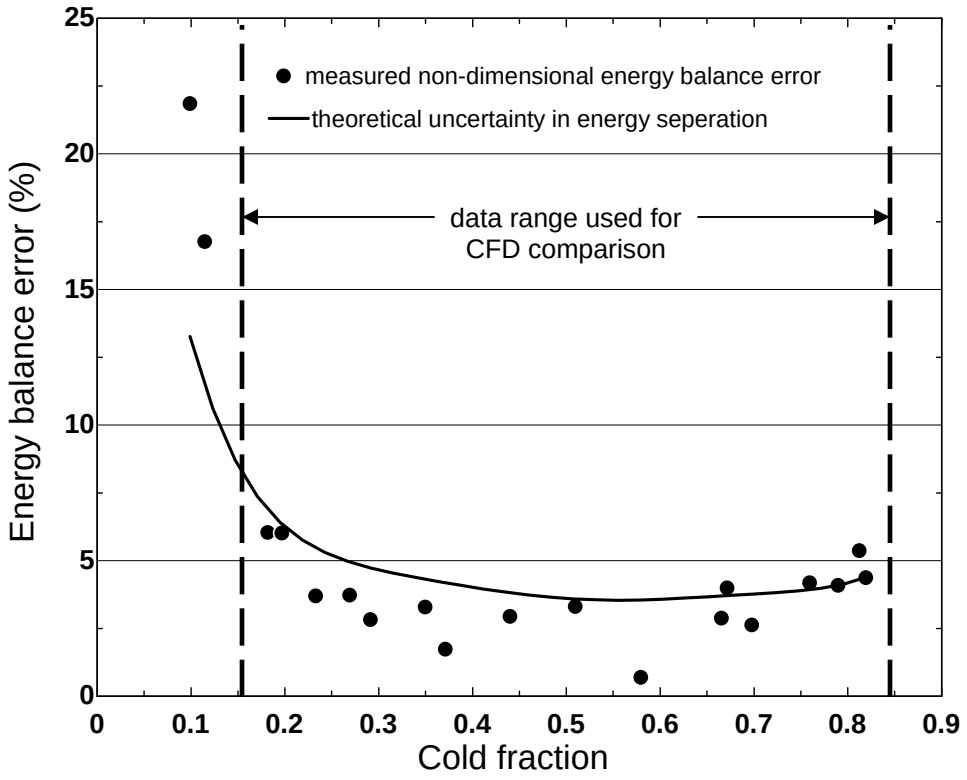

Figure 2: The theoretical uncertainty in the energy balance and the measured, non-dimensional energy balance error as a function of the cold fraction.

Notice that the theoretical uncertainty in the energy balance, which is based on the characteristics of the instruments, and the measured non-dimensional energy balance error, which is calculated from the data,

exhibit similar trends. Only those data with a measured, non-dimensional energy balance error of less than 10% are subsequently used to compare with the CFD results. Data corresponding to cold fractions between 0.18 and 0.82 satisfy this criterion and typically show energy balance errors of less than 5%; these data lie between the vertical lines shown in Fig. 2.

Table 1: Range and accuracy of the equipment used in the test setup.

Lab Equipment

Reference	Range	Uncertainty
Rotameter 1, 2.2, 3.2	30-290 (liters/min)	2% F.S.
Rotameter 2.1,3.1	60-570 (liters/min)	2% F.S.
Analog Pressure Gauge 1	0-690 kPa (gauge)	1% F.S.
Analog Pressure Gauge 2	0-210 kPa (gauge)	3.4 kPa
Analog Pressure Gauge 3	0-690 kPa (gauge)	1% F.S.
Thermopile Junction 1	N/A	0.35 C
Thermopile Junction 2	N/A	0.28 C
Thermistor 1,2,3	-40 to 100 C	0.1 C
Nozzle Pressure Tap	0-690 kPa (gauge)	0.5% FS

3. Experimental Vortex Tube Geometry

A picture and schematic of the vortex tube are shown in Figs. 3 and 4. The 10.6 cm working tube length is the section where the power separation occurs, and it was used as the bounding geometry for the CFD model.

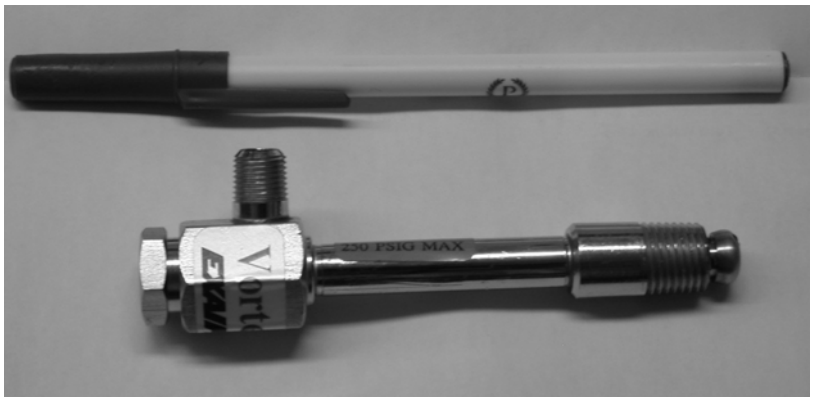

Figure 3: Picture of vortex tube used for experiment

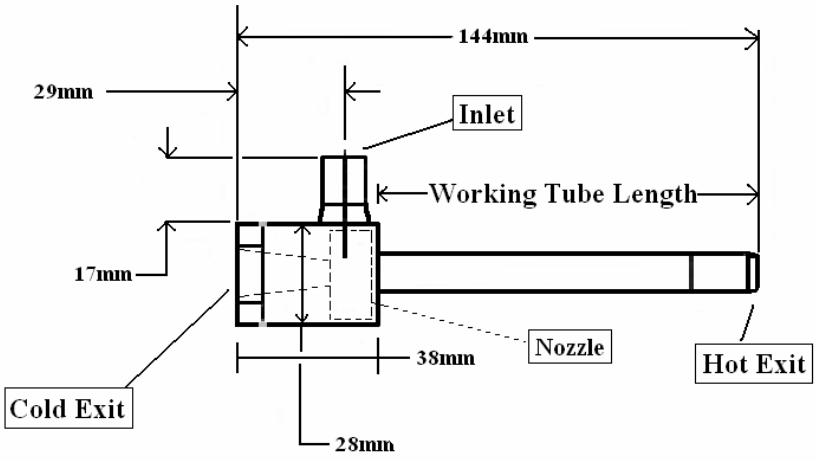

Figure 4: Schematic of vortex tube

The cold and hot exits are axial orifices with areas of 30.2 mm^2 and 95.0 mm^2 respectively, as measured with a micrometer. The nozzle of the vortex tube consists of 6 straight slots that direct the flow to high tangential velocities. The dimensions of the nozzle were measured using digital pictures of the nozzle taken with a scale, as shown in Figure 5. The scale is compared to pixel length and used to convert from pixel measurements to millimeters. The height of each slot is 0.97 mm, the width is 1.41 mm, and the length is 3.07 mm. The total area normal to the flow (A_n) associated with six nozzles is therefore 8.15 mm^2. The geometric measurements of the vortex tube are summarized in Table 2.

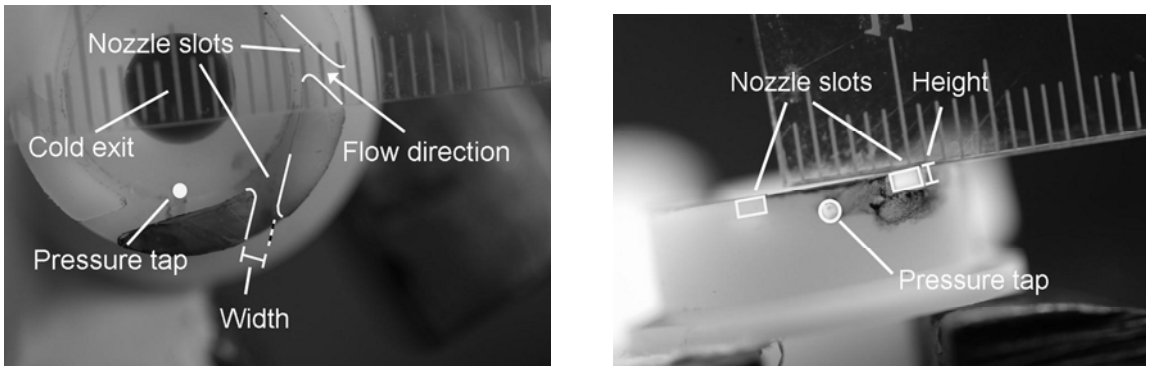

(a) (b)

Figure 5: (a) Top view of nozzle, used for measuring width, and (b) front view of nozzle, used for measuring height.

Nozzle inlet vectors are defined using the convention shown in Fig. 6 where V_n represents the total velocity vector, while V_r and V_θ denote the radial and tangential components of velocity, respectively.

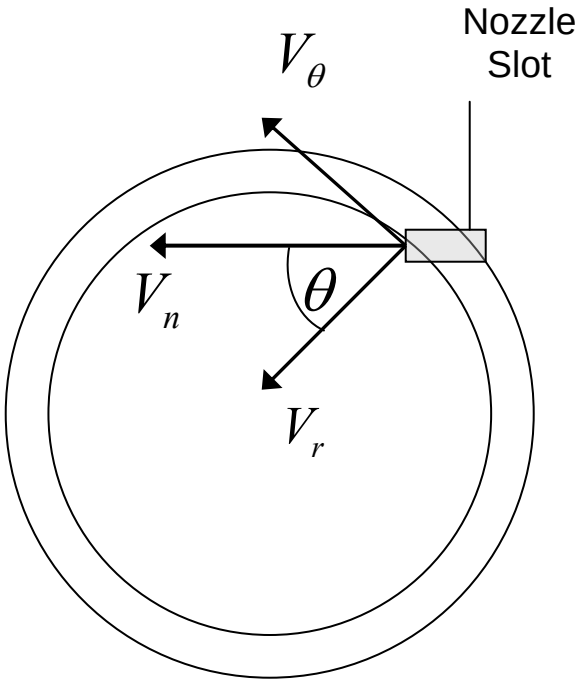

Figure 6: Radial and tangential components of velocity vector

The magnitudes of the vector components were measured using digital photographs of the nozzle, as shown in Fig. 7. The angle θ was calculated using the measured values of L1 and L2 shown in Fig. 7; L1 represents the distance along a line in arbitrary units between the center of the nozzle and a perpendicular intersection to the centerline of the slot that forms the nozzle, while L2 is the distance between the perpendicular intersection and the estimated location of the nozzle inlet in the same units. The velocity components are then defined as:

$$V_r = V_n \cos(\theta) \tag{6}$$

$$V_\theta = V_n \sin(\theta) \tag{7}$$

where

$$\theta = \arctan\left(\frac{\mathrm{L1}}{\mathrm{L2}}\right) \tag{8}$$

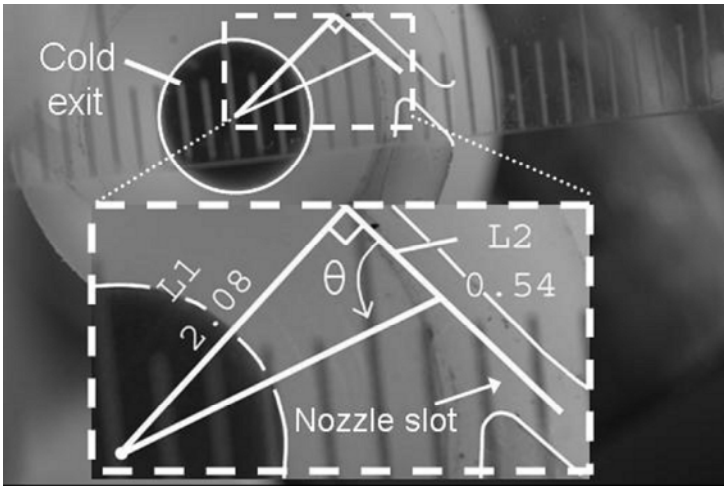

Figure 7: Measurement of inlet nozzle vector

The uncertainty in the angle θ is primarily associated with defining the nozzle inlet position, or the value of L1 in Fig. 7; the uncertainty in angle θ is tabulated in Table 2.

Table 2: Geometric measurements of the vortex tube.

Vortex Tube Geometry Summary

Measurement	Value	Uncertainty
Working Tube Length	10.6 cm	0.1 cm
Working Tube I.D.	1.14 cm	0.01 cm
Nozzle Height	0.97 mm	4.5%
Nozzle Width	1.41 mm	4.5%
Nozzle Total Inlet Area (A_n)	8.2 mm^2	7%
Cold Exit Diameter	6.2 mm	1.4%
Cold Exit Area	30.3 mm^2	3%
Hot Exit Diameter	11.0 mm	0.1 mm
Hot Exit Area	95 mm^2	4%
L1	2.08	1%
L2	0.54	1%
Theta (Y)	75.48	9%
Tangential Velocity (V_θ)	0.97 V_n	± 0.03 V_n
Radial Velocity (V_r)	0.25 V_n	± 0.11 V_n

4. CFD Model

The FLUENT™ software package was used to create the CFD model of the working length of the vortex tube pictured in Fig. 4. The model is two-dimensional, axisymmetric (with swirl), steady state, and employs the standard k-epsilon turbulence model. A complete list of the model parameters can be found in Appendix 2. The RNG k-epsilon turbulence model was also investigated, but resulted in a decrease in the model accuracy relative to the experimental data. More advanced turbulence models such as the Reynolds stress equations could not be made to converge for this simulation. The geometric model was created using the measured dimensions of the vortex tube in order to specify the length and radius, as well as the areas of the inlet and exit ports. The inlet is modeled as a continuous annular opening, which is slightly different than the 6 discrete nozzles in the experimental vortex tube. Additionally, the CFD models the hot exit as an annular outlet, while Exair vortex tube has an axial outlet. A mesh consisting of 25,000 grid points shown in Fig. 8 was used with node concentration near the orifices. Because of the symmetry of the vortex tube, the model was defined as half of the cross section of the vortex tube as pictured in Fig. 9.

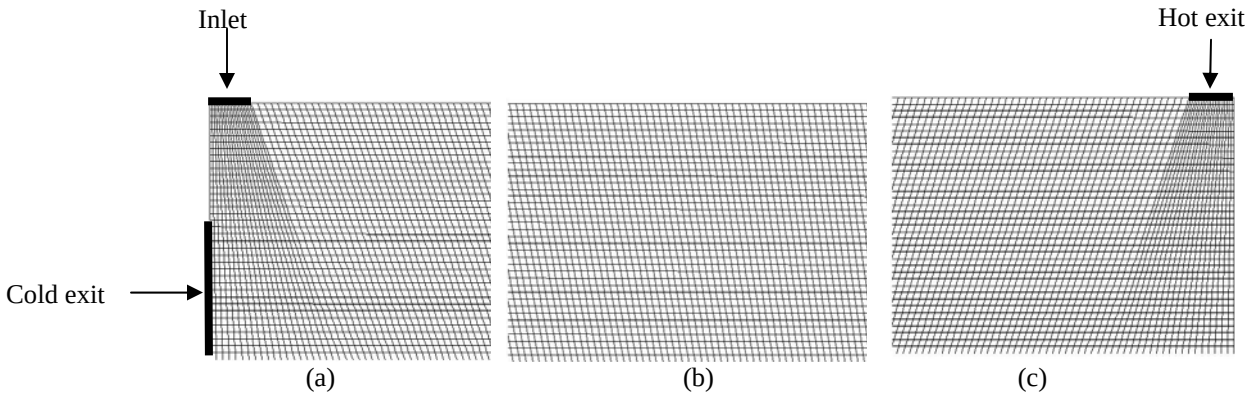

Figure 8: CFD mesh grid showing node distribution at the (a) inlet/cold exit, (b) mid-section, and (c) hot exit

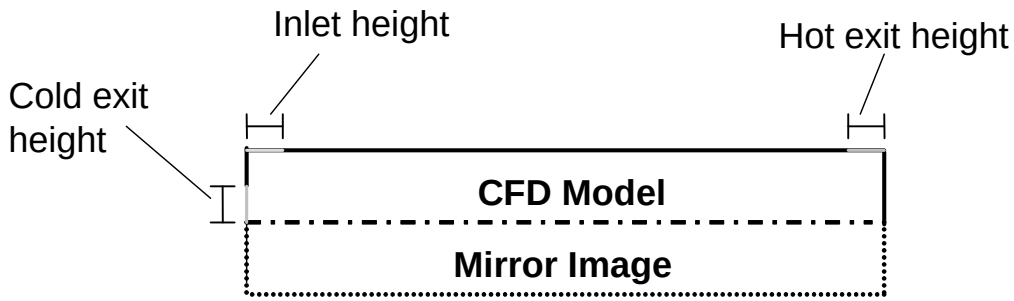

Figure 9: Schematic of the CFD model, shown with mirror image for clarity

Boundary conditions for the model were determined based on the experimental measurements. The inlet is modeled as a mass flow inlet; the total mass flow rate, stagnation temperature, and direction vector were specified. The hot and cold exits are represented as pressure outlets using measured values of the static pressure. A no-slip boundary condition is enforced on all walls of the vortex tube.

The inlet boundary represents the exit of the nozzle, and is located on the far left side of the top edge in the CFD model. The inlet operating conditions associated with the vortex tube experiments were nearly constant. The volumetric flow rate varied between 6.2 cfm and 6.3 cfm, the stagnation pressure varied between 67.5 psig and 68.5 psig, and the stagnation temperature varied between 21.1°C and 21.3°C. Therefore, the inlet mass flow rate varied between 8.26 and 8.43 g/s. Since these variations are small, average values of the measured inlet mass flow rate and stagnation temperature were used to specify the inlet boundary conditions for the CFD model.

The flow enters the experimental vortex tube through 6 discrete nozzle slots; however, in the CFD model, the inlet was modeled as an annular inlet. The area of the CFD annular inlet was specified in order to provide the correct tangential velocity and total mass flow rate. Additionally, in the CFD model, only the radial component of velocity contributes to the mass flow into the vortex tube. Therefore, the continuity equation requires that

$$V_n A_n = A_m V_r \tag{9}$$

where A_n is the total normal experimental nozzle area (measured), and A_m and is the inlet area for the model. Substituting Eq. (6) into Eq. (9) leads to:

$$A_m = \frac{A_n}{\cos(\theta)} \tag{10}$$

At low cold fractions, the CFD model predicts that reversed flow will occur at the cold exit, as shown in Fig. 10. Therefore, a backflow temperature must be specified for the reversed flow. The backflow temperature was calculated using two different techniques. The first used a velocity-weighted-average of total temperature of the flow leaving the cold exit. The second technique was an iterative method in which the backflow temperature was adjusted in order to minimize the overall energy balance error for the CFD model. The backflow temperature values that result from using these two techniques differed by about 7 K; however, the cold exit temperature predicted using these two methods differed by only 0.1 K, so either method is considered acceptable. The iterative method was utilized for the data reported here.

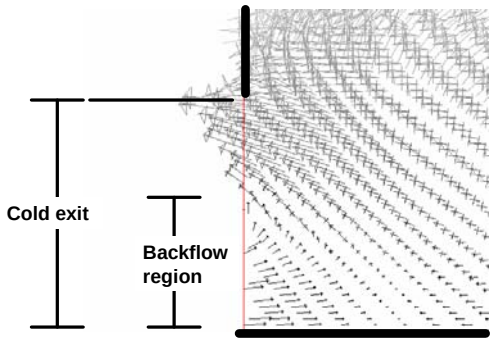

Figure 10: Reversed flow through cold exit at low cold fraction

In the CFD model, the hot exit was defined as a radial exit with a specified static pressure. The radial exit configuration is different from the axial exit associated with the experimental vortex tube; however, the flow distribution in the hot exit region has a negligible effect on the performance of a reasonably long vortex tube, and the CFD model was unable to converge when an axial exit was modeled. Figs. 11 (a) and (b) show the streamlines in the r-x plane associated with the flow inside the vortex tube.

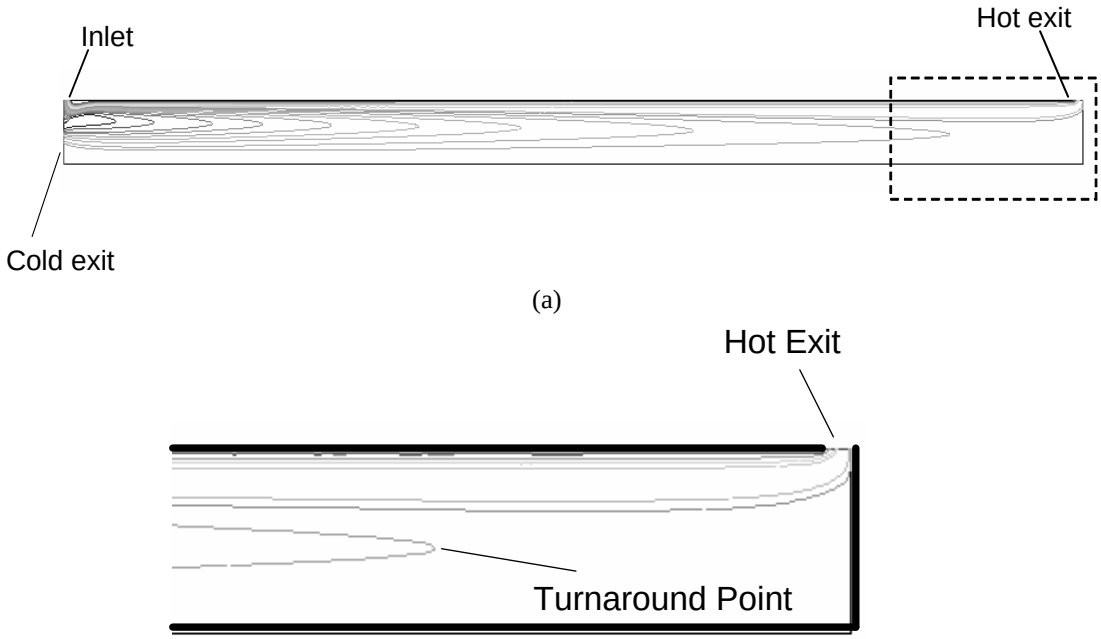

Figure 11: (a) Streamlines for entire vortex tube in *r-x* plane and (b) detailed view of streamlines near the hot exit

Notice that the interaction between the gas streams leaving the cold and hot exits is complete a significant distance before the hot exit. Therefore, in the CFD model the majority of power separation occurs before this point as noted by Aljuwayhel et al. [5]. Any change in the orientation of the hot exit geometry therefore has little effect on the separation effect calculated by the model provided that (a) the tube length extends beyond the turnaround point shown in Fig. 11 and (b) the hot exit represents an orifice with a flow resistance equivalent to the actual hot exit.

5. Comparison between CFD and Experiment

The CFD model described thus far is compared to the measured data gathered from the commercial vortex tube. Emphasis is placed on temperature and energy separation, as these measurements have the highest degree of confidence for performance comparison. Measurements of pressure are also reported, but are not rigorously used for model verification. Additionally, model sensitivities to turbulence model and inlet area are analyzed.

All comparisons between the model and the measured data are reported in terms of the cold fraction. In the experiment, the cold fraction is directly related to the pressure at the hot exit, as seen in Fig. 12. In addition, changing the hot exit pressure caused the cold exit pressure to change due to the pressure drop associated with the additional flow through the cold orifice as shown in Fig 12. To operate the vortex tube with cold fractions lower than 0.4, it was necessary to increase the cold exit pressure which was accomplished using the valves on the cold exit rotameters; the increase in the cold exit pressure results in a corresponding increase in the hot exit pressure. In the CFD model, the cold exit pressure boundary condition was specified at the measured cold exit pressure, and the hot exit pressure was iteratively specified until the experimentally measured cold fraction was achieved. As seen in Fig. 12, the model generally over-predicted the hot exit pressure required for a given cold fraction, however the general trend agrees well. The model consistently over-predicted the hot exit pressure by about 20 kPa for data with cold fractions between 0.37 and 0.75.

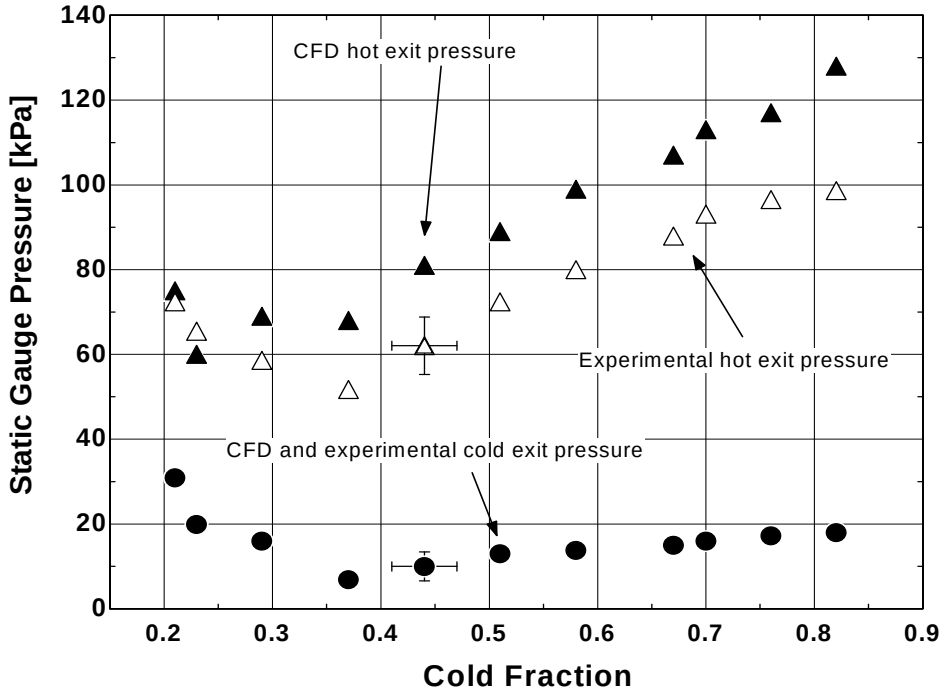

Figure 12: Experimentally measured and CFD model predictions of hot and cold exit static pressure as a function of the cold fraction

Since the vortex tube has no external source of work or heat, the power separation process is driven only by the availability associated with the high pressure air supplied to the inlet. The CFD model predicts the total pressure at the inlet that is required given the flow rate, total temperature, and inlet area specified as boundary conditions. The mass-weighted-averages of the total inlet pressure predicted by the CFD model are shown in Fig. 13 as a function of the cold fraction; the experimentally measured values of inlet pressure are also shown in Fig. 13. Note that these pressure values should not exactly agree as the definition of the total inlet pressure in the CFD model implies the pressure that would exist if the inlet flow were isentropically decelerated to zero velocity (i.e., if the nozzle was reversible) whereas the actual nozzle is relatively crude and therefore clearly irreversible. Because the inlet stagnation pressure is experimentally measured upstream of the irreversible nozzle, it should be higher than the total pressure at the inlet predicted by the CFD model. Fig. 13 illustrates that the model consistently predicts that the inlet total pressure is about 120 kPa lower than the measured inlet pressure. However, the difference between these two pressure values is too large to account for irreversible flow in the nozzle. Therefore, the model was later altered to increase the inlet total pressure; the results of this modification are reported in the Conclusions.

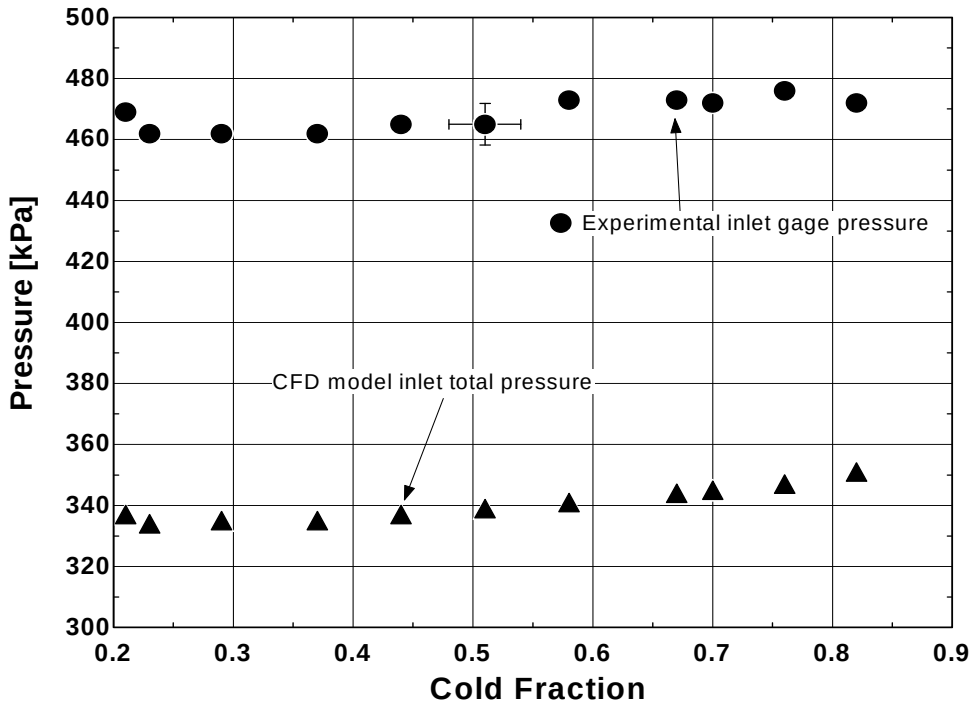

Figure 13: Experimentally measured inlet pressure and the total inlet pressure predicted by the CFD model as a function of the cold fraction

The temperature separation measured by the experiment and predicted by the CFD model is the absolute difference between the inlet temperature and the respective exit temperatures. The inlet temperature in the CFD model was specified as a constant 294.2 K which is consistent with the measured total temperature at the inlet to the vortex tube. Fig. 14 shows the measured and predicted hot and cold temperature separation as a function of the cold fraction. The model consistently under-predicts the cold and hot temperature separation by approximately 16 K and 4 K, respectively.

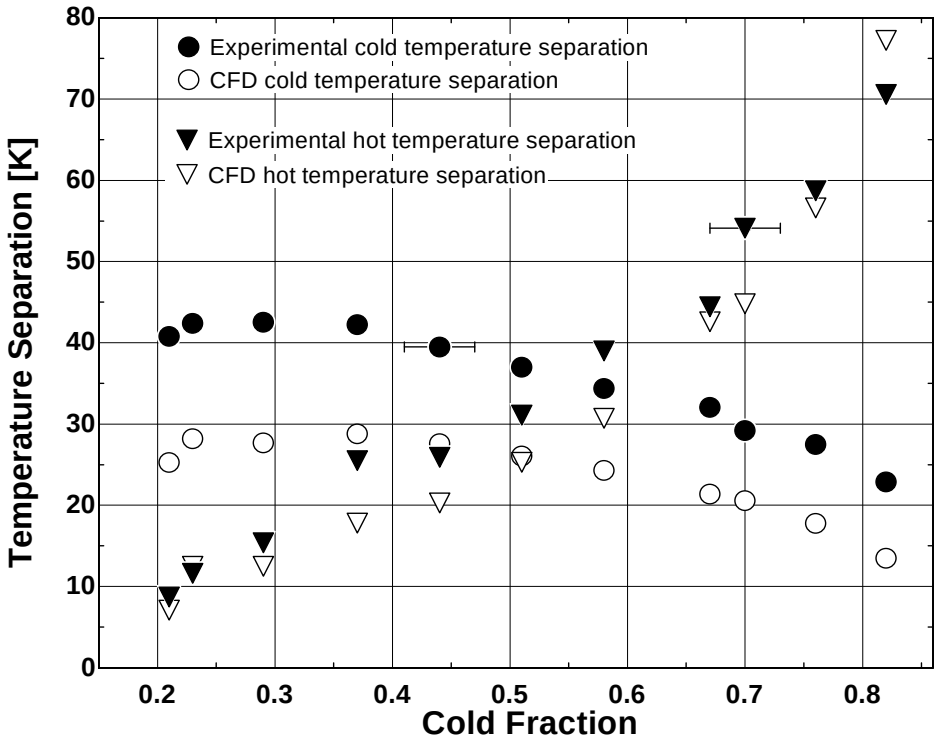

Figure 14: Experimentally measured and predicted hot and cold temperature separation as a function of cold fraction

The rate of energy separation provides another measure of the vortex tube performance. The rates of energy separation ($\dot{Q}_h$ and $\dot{Q}_c$) were calculated using Eqs. (1) and (2) based on the experimental data and the CFD predictions, and are shown in Fig. 15 as a function of the cold fraction. Again, the model consistently under-predicts the separation effect in the vortex tube, however the shape of the curve and the qualitative trends agree very well. Both the experimental data and the model show maximum power separation with a cold fraction of about 0.65.

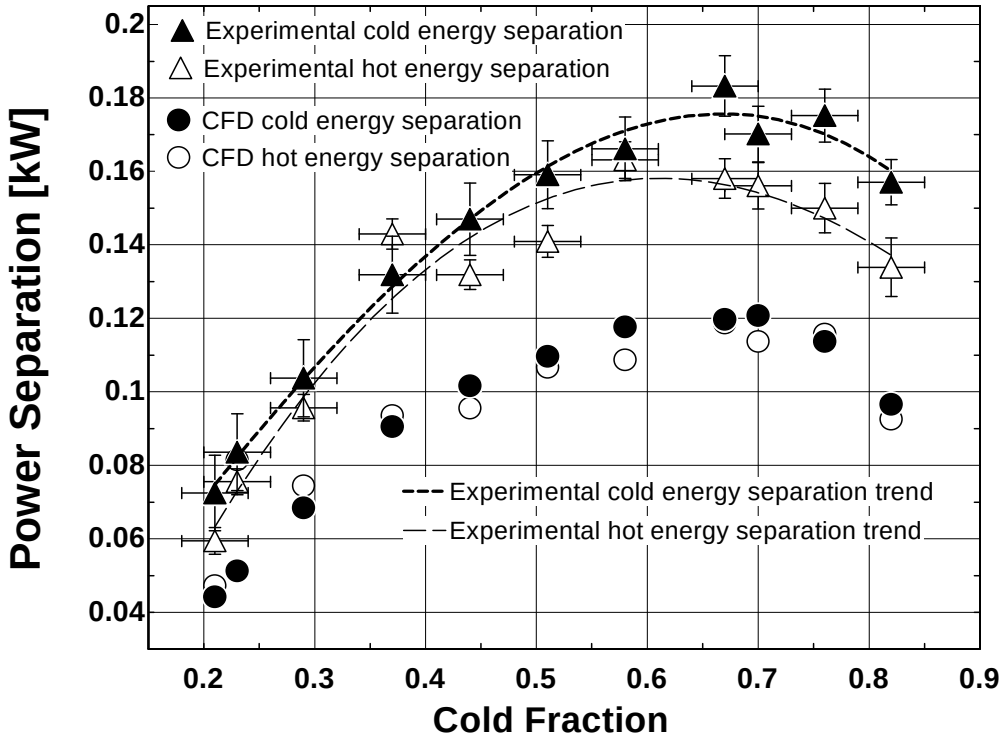

Figure 15: Experimentally measured and predicted hot and cold power separation rate as a function of cold fraction

Alternate turbulence models were explored in an attempt to improve the model predictions. The first change was from the standard k-epsilon equations to the RNG k-epsilon equations. This change increased the discrepancy between the experimental measurements and CFD predictions for power separation, as shown in Fig 16. When the Reynolds-stress turbulence model was employed, FLUENT™ was unable to produce reasonable results. In these cases, the CFD program showed hot flow leaving the cold exit and cold flow leaving the hot exit. In addition, the energy residual values did not converge to acceptable values considering the observed magnitudes of power separation.

The comparisons between model and experiment described above were based on measured boundary conditions and measured geometric characteristics. Of these measurements, the use of the measured inlet area provides the largest source of error. Altering the inlet area of the CFD model significantly affected the total pressure of the incoming compressed air. Because the total inlet pressure is a main factor contributing the magnitude of power separation within the vortex tube, the inlet area was changed to increase the CFD total inlet pressure to values closer to the experimentally measured inlet pressures. With a 23% decrease in

area, the CFD model predicted total inlet pressures that are comparable to the experimentally measured inlet pressures. Additionally, the predicted power separation increased significantly to values within 20% of the experimental measurements, as pictured in Fig. 16. The increased power separation was expected using the higher total inlet pressures as the availability of the incoming air subsequently increased.

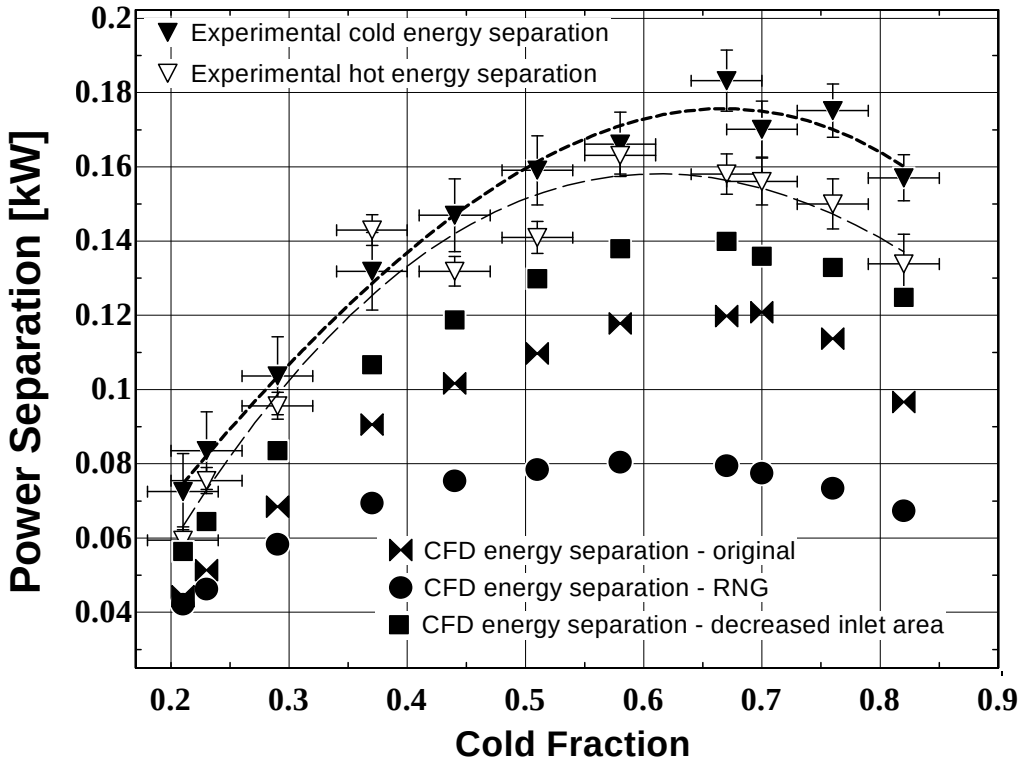

Figure 16: Experimentally measured and predicted power separation for the original CFD model, the CFD model with the RNG k-epsilon turbulence model, and the CFD model with a reduced inlet area

In addition to the inaccuracy of the inlet area measurement, the need to decrease the CFD models' inlet area may also be partially accounted for by boundary layer effects. The nozzle slots are relatively long in the flow direction and therefore it is likely that a significant boundary layer develops within the nozzle, resulting in an appreciable amount of blockage. As a result, it is likely that the effective area of the nozzle is less than the geometrically measured area of the slots.

6. Conclusion

The purpose of this research was to create a CFD model of a commercial vortex tube for use as a design tool in optimizing vortex tube performance. The model was developed using a two-dimensional (2-D)

steady axisymmetric model (with swirl) that utilized the standard k-epsilon turbulence equations. The RNG k-epsilon turbulence model was investigated; however, it was found to increase the difference between the measured and predicted energy separation.

The comparison between the CFD model and the measured experimental data yielded promising results relative to the model's ability to predict the power separation. When the original model was altered by reducing the inlet area it would found that the total inlet pressure compared favorably to the measured inlet pressure and the model predicted power separation values that were within 20% of the experimentally measured power separation. This trend is valid for the entire range of cold fraction and can partially be explained physically by considering boundary layer effects in the nozzle. The model also accurately predicts the maximum power separation operation point with respect to the cold fraction.

Since the model reasonably predicts the quantitative results for experimental power separation, it can be confidently used to further investigate parameters affecting vortex tube performance. Studies of interest that can be performed with the model include performance with different fluids, inlet temperatures and pressures, nozzle angles, and tube geometries. Investigating these parameters computationally is far less time consuming and costly than manufacturing and testing design variations. In this context, the model is useful as a time saving and cost effective tool for designing vortex tubes.

Acknowledgements

The authors thank Nawaf Aljuwayhel and Mohamed El-Morsi for their help in using FLUENT™ and CONDOR. Acknowledgment is made to the Donors of the American Chemical Society Petroleum Research Fund and the Hilldale Foundation for partial support of this research.

References Cited

1. W. Frohlingsdorf, and H. Unger, Numerical Investigations of the Compressible Flow and the Energy Separation in the Ranque-Hilsch Vortex Tube, International Journal of Heat and Mass Transfer, Vol. 42 (1999) 415-422.
2. H. H. Bruun, Experimental Investigation of the Energy Separation in Vortex Tubes, Journal of Mechanical Engineering Science 11 (No. 6) (1969) 567-582.
3. B. Ahlborn, J. U. Keller, R. Staudt, G. Treitz, and E Rebhan, Limits of temperature separation in a vortex tube, J. Phys D: Appl. Phys. 27 (1994) 480-488
4. B. Ahlborn, J. Camire, J.U. Keller, Low-pressure vortex tubes, J. Phys D: Appl. Phys. 29 (1996) 1469-1472
5. N.F. Aljuwayhel, G.F. Nellis, and S.A. Klein, "Parametric and internal study of the vortex tube using a CFD model," International Journal of Refrigeration, Vol. 28, No. 3, (2005), pp. 442-450.

Appendix 1 - Raw Data

Experimental data

Volumetric Flow [liters/s]			Temperature [C]			Gauge Pressure [kPa]		
Inlet	Cold Exit	Hot Exit	Inlet	Cold Exit	Hot Exit	Inlet (total)	Cold Exit (static)	Hot Exit (static)
1.22	3.53	3.57	21.3	-12.9	60.2	473	13.79	79.98
1.24	4.21	3.03	21.3	-10.5	65.6	472.3	15.86	87.91
1.24	4.17	2.77	21.4	-9.1	69.2	473	17.24	91.7
1.23	4.36	2.47	21.4	-7.7	75.2	472.3	15.17	93.08
1.22	4.78	2.20	21.4	-5.8	79.1	475.7	15.86	96.53
1.22	5.15	1.98	21.4	-4.3	83.8	474.4	17.24	96.53
1.23	5.03	1.79	21.3	-2.7	88	473	17.93	98.6
1.22	5.22	1.62	21.3	-1.2	91.8	471.6	17.93	98.6
1.25	1.26	5.58	20.6	-20.3	29.5	468.8	31.03	72.39
1.25	3.11	3.74	21.1	-15.9	52.1	465.4	13.1	72.39
1.25	2.66	4.21	21.1	-18.5	46.4	465.4	10.34	62.05
1.25	2.21	4.63	21.1	-21.3	46.9	461.9	6.895	51.71
1.25	1.73	5.14	21.1	-21.7	35.8	461.9	15.86	58.61
1.25	1.39	5.32	21.1	-21.5	32.1	461.9	19.99	65.5

Appendix 2 - Summary of CFD Model Parameters

Table 2a – CFD model geometry

Geometric Model

Dimension	Value
Inlet Height	0.7 mm
Inlet Area	32.5 mm^2
Cold Exit Diameter	6.2 mm
Cold Exit Area	30.25 mm
Hot Exit Height	1 mm
Hot Exit Area	35.81 mm^2
Length	10 cm
Tube I.D.	11.4 mm

Table 2b – Inlet boundary conditions

Inlet - Mass Flow Inlet

Boundary Condition	Value
Mass Flow	8.35 e-03 kg/s
Total Temperature	294.2 K
Supersonic/Initial Gauge Pressure	120000 Pa
Axial Velocity	0
Radial Velocity (V_r)	-0.25 V_n
Tangential Velocity (V_θ)	0.97 V_n
Inlet Area	25.1 mm^2
Turbulence Specification Method	Intensity and Hydraulic Diameter
Turbulence Intensity	5%
Hydraulic Diameter	0.1 cm

Table 2c – Cold exit boundary conditions

Cold Exit - Pressure outlet

Boundary Condition	Value
Gauge Pressure	Varies
Backflow Total Temp	Varies
Backflow Direction Specification Method	From Neighboring Cell
Turbulence Specification Method	Intensity and Hydraulic Diameter
Backflow Turbulence Intensity	5%
Backflow Hydraulic Diameter	0.3

Table 2d – Hot exit boundary conditions

Hot Exit - Pressure Outlet

Boundary Condition	Value
Gauge Pressure	Varies
Backflow Total Temp	325 K
Backflow Direction Specification Method	From Neighboring Cell
Turbulence Specification Method	Intensity and Hydraulic Diameter
Backflow Turbulence Intensity	5%
Backflow Hydraulic Diameter	0.15